

Enlarged magnetic focusing radius of photoinduced currents in mesoscopic circuits

Markus Stallhofer,¹ Christoph Kastl,¹ Marcel Brändlein,¹ Dieter Schuh,² Werner Wegscheider,³ Jörg P. Kotthaus,⁴ Gerhard Abstreiter,¹ and Alexander W. Holleitner¹

¹Walter Schottky Institut and Physik-Department, Technische Universität München, Am Coulombwall 4a, D-85748 Garching, Germany

²Institut für Experimentelle und Angewandte Physik, Universität Regensburg, D-93040 Regensburg, Germany

³Laboratorium für Festkörperphysik, HPF E 7, ETH Zürich, Schafmattstr. 16, 8093 Zürich, Switzerland

⁴Ludwig-Maximilians Universität München and Center for Nanoscience, Geschwister-Scholl-Platz 1, D-80539 München, Germany

(Received 12 January 2012; published 10 September 2012)

We use GaAs-based quantum point contacts as mesoscopic detectors to analyze the flow of photogenerated electrons in a two-dimensional electron gas at a perpendicular magnetic field. Whereas charge transport experiments always measure the classical cyclotron radius, we show that this changes dramatically when detecting the photoinduced nonequilibrium current in magnetic fields. The radius of the photocurrent flow patterns surprisingly exceeds the classical cyclotron value by far, both in experiment and Monte Carlo simulations. We identify electron-electron scattering as the underlying reason.

DOI: 10.1103/PhysRevB.86.115315

PACS number(s): 73.23.Ad, 42.82.Fv, 81.07.St, 85.35.Be

I. INTRODUCTION

In the presence of a magnetic field \mathbf{B} , propagating charge carriers obey the Lorentz force and move on curved trajectories in the plane perpendicular to the field. The corresponding classical cyclotron radius

$$r_{\text{cycl}}(|\mathbf{B}|) = \frac{m|\mathbf{v}|}{q|\mathbf{B}|} \quad (1)$$

for a charge q is a measure of its momentum and thus contains both mass m and velocity \mathbf{v} of the carrier. Based on Eq. (1), cyclotron resonance experiments on two-dimensional electron systems have been used to verify the two-dimensional nature, to determine the components of the effective mass tensor in solids, and to obtain information on Fermi contours.¹ However, following Kohn's theorem, the mass measured in cyclotron resonance experiments is expected to be the bare mass, not affected by electron-electron interactions.² In magnetic focusing experiments, quantum point contacts (QPCs) have been used both as injectors and detectors to indirectly obtain information on cyclotron trajectories of ballistic currents in two-dimensional electron gases (2DEGs).³⁻⁶ At 2DEG boundaries, even skipping cyclotron orbits have been visualized^{7,8} using a scanning gate technique,^{9,10} and different electron trajectories have been shown to interfere with each other.^{8,11-13} The extracted trajectories were in accordance with Eq. (1) and the expected effective mass m_{GaAs}^* of the GaAs-based circuits.

Here, we use an optical beam induced current (OBIC) technique to directly analyze the flow patterns of photogenerated electrons in a 2DEG embedded in an AlGaAs/GaAs quantum well at a perpendicular magnetic field. In contrast to the magnetic focusing results gained from transport experiments, we uncover the magnetic focusing dynamics of photogenerated nonequilibrium excess charge carriers in a 2DEG. A laser locally creates charge carriers at a certain position in the 2DEG, and the photocurrent of the photogenerated electrons across an adjacent QPC is measured as a function of the laser position.^{14,15} This OBIC technique allows adjusting the excitation position independent of the applied $|\mathbf{B}|$. Thus, it is possible to directly map the magnetic flow patterns of photogenerated

electrons in the 2DEG. We observe curved photocurrent flow patterns with a radius being inversely proportional to $|\mathbf{B}|$ as expected from Eq. (1). However, the measured radii are 10 to 30 times larger than anticipated. Peculiarly, assuming Eq. (1) and the given electron Fermi velocity v_{Fermi} in the 2DEG, a factor of 30 would suggest an electron mass for the GaAs quantum well which is up to two times larger than the vacuum value m_e , with $30m_{\text{GaAs}}^* = 30 \times 0.067m_e \approx 2m_e$. We discuss underlying scattering processes of the photogenerated electrons and identify electron-electron scattering to explain the findings.¹⁶⁻¹⁸ The interpretation relies on the observed laser power dependence, i.e. a larger effective radius for a higher laser intensity. We perform Monte Carlo simulations of the effective radius of the trajectory of photogenerated excess electrons in a perpendicular magnetic field at the presence of small-angle scatterers. We find very good agreement between the simulations and the data. Our findings suggest that due to an enhanced influence of electron-electron scattering, the radius of the trajectories of hot electrons is generally enlarged as compared to Eq. (1). Our observations underline the predominant influence of electron-electron scattering processes in mesoscopic and nanoscale photodetectors.

II. EXPERIMENTAL PROCEDURE

The starting point is an AlGaAs/GaAs heterostructure with a 25-nm-wide GaAs quantum well 95 nm below the surface. The quantum well comprises a 2DEG with a Fermi energy $E_{\text{Fermi}} = 9.83$ meV and an electron mobility of $\mu = 1.74 \times 10^6$ cm²/Vs. The elastic mean free path l_{mfp} is determined to be 15.1 μm at $T = 4.2$ K. Generally, l_{mfp} is the average length scale, at which majority charge carriers can propagate without momentum scattering. In GaAs-based heterostructures at low temperatures, l_{mfp} is mostly limited by long-range scatterers. As sketched in Fig. 1(a), QPCs are lithographically defined by shallow etching two circles with a radius of $r_{\text{circuit}} = 15$ μm defining an electronic constriction with an electronic width of ~ 50 nm, which is comparable to the Fermi wavelength $\lambda_{\text{Fermi}} = 48$ nm.¹⁴ On both ends of this QPC, the remaining 2DEG acts as source and drain. The QPC is covered with an opaque gold topgate with a

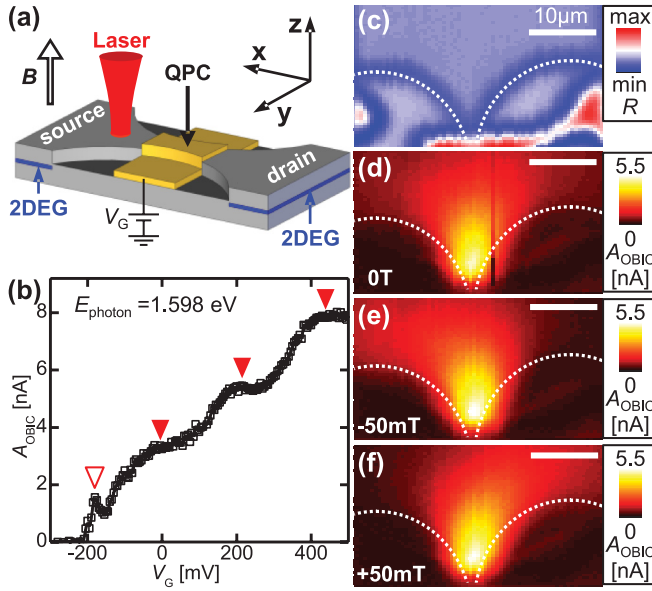


FIG. 1. (Color online) (a) Sketch of a quantum point contact (QPC) with an opaque topgate, a laser excitation in the 2DEG section acting as source, and a perpendicularly applied magnetic field B . The photocurrent is detected at drain. (b) A_{OBIC} as function of V_G . Quantization steps reveal one-dimensional subbands (filled triangles) ($V_{\text{SD}} = -2.5$ mV, $E_{\text{ph}} = 1.598$ eV, $P_{\text{laser}} = 0.54$ μ W, $|B| = 0$ T). (c) Spatially resolved reflection map. Spatial map of A_{OBIC} for (d) 0 T, (e) -50 mT, and (f) 50 mT ($V_{\text{SD}} = -2.5$ mV, $V_G = 60$ mV, $E_{\text{ph}} = 1.598$ eV, $P_{\text{laser}} = 1.0$ μ W).

lateral width in the x direction of 8 μm , and the topgate is connected to a voltage V_G . The sample is placed inside a confocal microscope in a helium bath cryostat at temperature $T = 4.2$ K. Without laser excitation, the low-temperature conductance across the QPC shows quantization steps of $2e^2/h$ (data not shown).^{3,4} The OBIC measurements are performed at photon energies of $E_{\text{ph},1} = 1.546$ eV and $E_{\text{ph},2} = 1.598$ eV. Here, $E_{\text{ph},1}$ corresponds to a quasi-resonant excitation of the quantum well, as proven by independent photoluminescence measurements (data not shown). For $E_{\text{ph},2}$, the photogenerated electrons exhibit an average excess energy of $\Delta E = 49$ meV above the Fermi energy, if one takes into account the energy portion transferred to the heavy holes in the valence band. The energetic FWHM of both lasers is 8 meV. Due to laser and current heating as well as heat radiation, the electron temperature is estimated to be 8–10 K.¹⁵

The position of the sample with respect to the laser is monitored by a resistive element on the nanopositioners (attocube ANPx101/Res) with a relative precision of approximately 200 nm. Between different measurements the repeatability precision of the absolute position is approximately 1 μm . While scanning the focused laser spot across the sample, we measure the optical beam induced current (OBIC) through the QPC depending on the excitation position with the current voltage amplifier being connected to a fast lock-in amplifier that is triggered to the laser repetition frequency of 40 MHz.

Generally, photogenerated electrons in the source contact propagate across the QPC before they are detected in drain. In contrast, photogenerated holes diffuse to a position near

the QPC due to the potential landscape. For a fixed excitation position with respect to the QPC, the amplitude of the OBIC shows clear quantization steps as a function of V_G [filled triangles in Fig. 1(b)]. The steps are interpreted to reflect the electronic one-dimensional subbands of the QPC. The peak at the onset of the first plateau [open triangle in Fig. 1(b)] can be explained by an interference effect¹⁹ or the influence of an impurity at the aperture of the QPC,^{20,21} and it is beyond the scope of this paper. Depending on the laser intensity and thus on the number of photogenerated holes accumulated around the QPC, the quantization steps are shifted with respect to the topgate voltage by a photoconductive gain effect. The process of hole accumulation and subsequent electron-hole recombination happens on a ms timescale.¹⁵ By this, the shift by the photoconductive gain effect can be regarded as quasistatic in all experiments at high laser trigger frequencies on the order of a few tens of MHz.¹⁴ Most importantly, for the measurements discussed in Figs. 2, 3, 4, and 5, the gate voltage V_G is chosen such that the QPC detects either at the first or second conductance plateau throughout all P_{laser} and positions of the laser, respectively.

III. EXPERIMENTAL DATA

By simultaneously detecting the OBIC and the reflected light from the sample [Fig. 1(c)], one can relate the spatial dependence of the photocurrent to the sample geometry. Figure 1(d) depicts a respective OBIC map at $|B| = 0$ T. The OBIC decays exponentially on a typical decay length l_{photo} comparable to l_{mfp} .¹⁴ At a moderate magnetic field, the OBIC signal is not symmetric anymore [Figs. 1(e) and 1(f)]. Experimentally, we find that for $|B| \geq 100$ mT, the minimum detectable radius of the flow patterns is limited by r_{circuit} . This can be understood such that the photogenerated electrons propagate in skipping orbits smaller than the laser spot size of ~ 2 μm along the circuit's boundary. In the following, we focus on magnetic fields with $|B| < 100$ mT, for which photogenerated electrons should propagate along cyclotron orbits with $r_{\text{cyclo}} > 0.87$ μm according to Eq. (1).

Such an OBIC map is depicted as dots in Fig. 2(a). The QPC is positioned at $(x, y) = (0, 0)$, and the topgate extends from -4 $\mu\text{m} \leq x \leq 4$ μm . The data are fitted by a 2D function:

$$h(x, y) := \exp\left(\frac{-[\sqrt{(x-x_c)^2 + (y-y_c)^2} - r_{\text{eff}}]^2}{2\{\sigma_0[1 + (\frac{r_{\text{eff}}\phi}{a_1})^{a_2}]\}^2}\right) * \Theta(\phi) \exp\left(-\frac{\phi r_{\text{eff}}}{l_{\text{photo}}}\right) \frac{1}{\sqrt{2\pi}\sigma_L} \exp\left[-\frac{(\phi r_{\text{eff}})^2}{2\sigma_L^2}\right], \quad (2)$$

with an effective radius r_{eff} and an angle ϕ denoting the polar coordinates of the circular trajectories. Here, $h(x, y)$ comprises two subfunctions. The first part considers a Gaussian distribution centered on a circle with radius r_{eff} around a midpoint (x_c, y_c) . Here, σ_0 represents the spatial width of the Gaussian distribution of the photogenerated electrons at the aperture of the QPC at $(x = 5$ $\mu\text{m}, y = 0)$, and the width widens along the trajectories as described by the parameters a_1 and a_2 . The second part of $h(x, y)$ represents the exponential

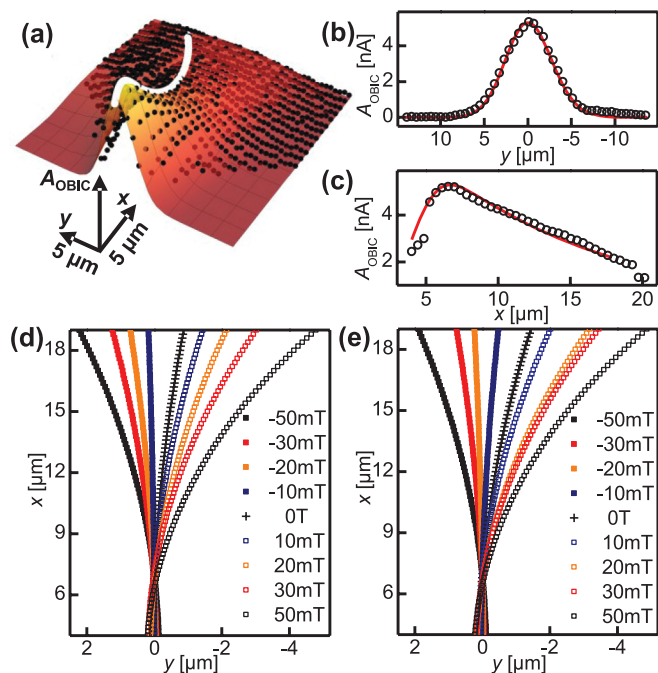


FIG. 2. (Color online) (a) A_{OBIC} map for quasi-resonant excitation (scattered black points) with two-dimensional fitting function ($E_{ph} = 1.546$ eV, $V_G = 0$ mV, $V_{SD} = -2.5$ mV, $P_{laser} = 1.0$ μW , $\mathbf{B} = -50$ mT). White line denotes cyclotron trace of maximum A_{OBIC} . (b) and (c) Typical cuts along x and y in an OBIC map with scattered data points and fitting function ($E_{ph} = 1.598$ eV, $V_G = 60$ mV, $V_{SD} = -2.5$ mV, $P_{laser} = 1.1$ μW , $\mathbf{B} = 50$ mT). (d) and (e) Cyclotron trajectories extracted from OBIC maps for the first ($V_G = 60$ mV) and second ($V_G = 250$ mV) quantization plateaus, respectively ($V_{SD} = -2.5$ mV, $P_{laser} = 1.1$ μW , $E_{ph} = 1.598$ eV).

decay of the OBIC amplitude.¹⁴ For the present magnetic focusing experiments, the decay needs to be considered along a bent trajectory starting at the onset of the opaque topgate, influenced by the spatial width of the Gaussian laser spot. This is implemented by defining a convolution of the exponential decay along the orbital coordinate $r_{eff}\phi$ with decay length l_{photo} multiplied with a Heaviside step function $\Theta(\phi)$ starting at $r_{eff}\phi = 0$, with a Gaussian distribution (centered at $r_{eff}\phi = 0$) with a width σ_L . The latter represents the laser spot size.

In order to demonstrate the very good agreement of $h(x, y)$ with the data, we depict Cartesian cuts along y at $x = 6 \mu\text{m}$ [Fig. 2(b)] and along x at $y = 0 \mu\text{m}$ [Fig. 2(c)]. We point out that the relevant parameters of the distribution such as the effective radius r_{eff} can be determined with accuracy much higher than the resolution of the confocal microscope, since the fit averages over the 2D ensemble of data points. The white line in Fig. 2(a) highlights the fitted circular orbit of the photogenerated electrons along the magnetic focusing trajectory. Such traces for varying \mathbf{B} are plotted in Figs. 2(d) and 2(e) for the QPC tuned to the first and second plateau, respectively. Surprisingly, the values for r_{eff} are approximately one order of magnitude larger than the classical cyclotron radius r_{cyclo} . For comparison, for $|\mathbf{B}| = 50$ mT, Eq. (1) gives $r_{cyclo} = 1.74 \mu\text{m}$, whereas we measure $r_{eff} = 32 \mu\text{m}$ for $E_{ph} = 1.546$ eV and $P_{laser} = 2.8 \mu\text{W}$. We emphasize that for $|\mathbf{B}| < 50$ mT, the trajectories are farther from the boundaries than

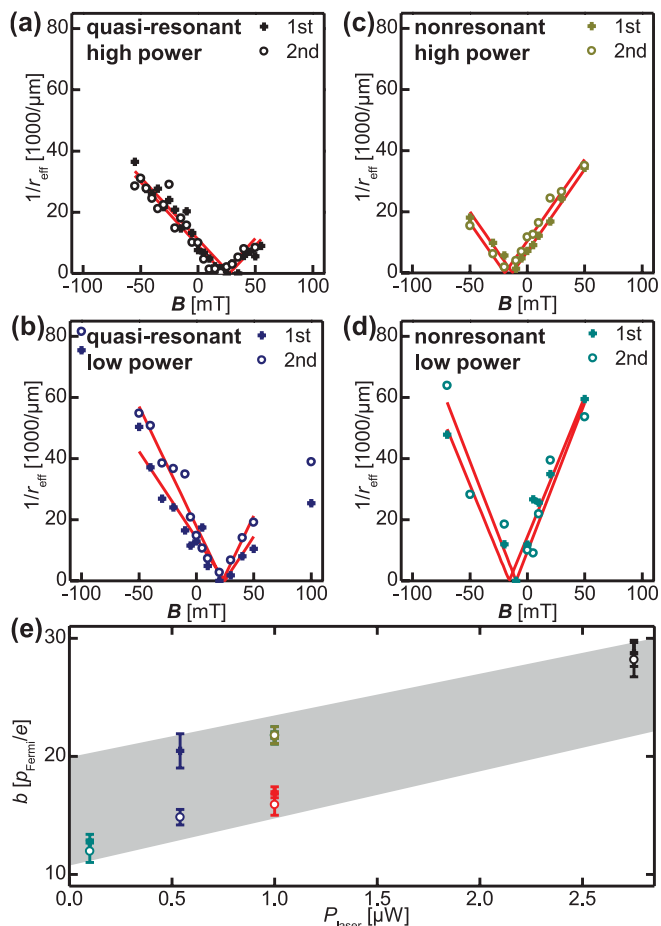


FIG. 3. (Color online) Inverse r_{eff} vs \mathbf{B} for the first (crosses) and second (circles) quantization plateau at (a) $E_{ph} = 1.546$ eV and $P_{laser} = 2.8 \mu\text{W}$, (b) $E_{ph} = 1.546$ eV and $P_{laser} = 0.54 \mu\text{W}$, (c) $E_{ph} = 1.598$ eV and $P_{laser} = 1.1 \mu\text{W}$, and (d) $E_{ph} = 1.598$ eV and $P_{laser} = 0.11 \mu\text{W}$. Lines are fits. (e) Fitting parameter b extracted from (a)–(d) as a function of P_{laser} . The two red (lower) symbols at $P_{laser} = 1 \mu\text{W}$ represent data for quasi-resonant excitation $E_{ph} = 1.546$ eV at $P_{laser} = 1.0 \mu\text{W}$.

both the laser spot size and the classical cyclotron radius. Thus, we can exclude skipping orbits and edge channels to explain the observation.

Figure 3 shows the inverse of r_{eff} vs \mathbf{B} for quasi-resonant excitation [Figs. 3(a) and 3(b)] and nonresonant excitation [Figs. 3(c) and 3(d)] for different P_{laser} . The data are shown as scattered points. The lines are fits according to Eq. (1) with $b = \frac{m^*|v|}{e} = \frac{|p|}{q}$ as a fitting parameter. Generally, assuming a ballistic cyclotron motion of single electrons after a quasi-resonant (nonresonant) excitation at $E_{Fermi} = 9.83$ meV, b can be estimated to be $b_{Fermi} = \frac{m^*v_{Fermi}}{e} = 87 \mu\text{m} \cdot \text{mT}$ ($b_{nonresonant} = 212 \mu\text{m} \cdot \text{mT} \approx 2.4b_{Fermi}$). For these approximations, we use the absolute value of the electron momentum $|p| = \sqrt{2m^*E}$, the effective electron mass of $m^* = 0.067m_0$, an energy $E = 9.8$ meV [$E = (49 + 9.8)$ meV], and the elementary charge e .

Generally, the applied magnetic field \mathbf{B} at the position of the samples in the cryostat is calibrated by the help of Hall probes independently of the presented experiments. In the data in Figs. 2(d) and 2(e) as well as Figs. 3(a) to 3(d),

however, an offset of the response of the QPC to the magnetic field axis is detectable. We interpret it to be caused by a slight asymmetry in the direct electrostatic environment of the source contact of the QPC or a scatterer in the vicinity of the QPC,^{10,20,22} varying for each cooldown of the sample. The two values $B_0 = +20$ mT in Figs. 3(a) and 3(b) and $B_0 = -15$ mT in Figs. 3(c) and 3(d) were taken from two different measurement periods in between which the sample was cycled to room temperature and back to liquid helium temperature. For low magnetic fields close to zero, it is difficult to tell if a certain trajectory is bent with a large radius or if it is just slightly kinked due to the effect of a possible scatterer. The underlying electrostatic environment might have been changed between the nonresonant and quasi-resonant measurements as the sample was heated to room temperature in between. By this, the two different offsets around $B_0 = +20$ mT [Figs. 3(a) and 3(b)] and $B_0 = -15$ mT [Figs. 3(c) and 3(d)] can be understood. In principle, the wave functions in QPCs favor certain k directions of electrons entering the QPC.^{9,10} In Figs. 3(a) to 3(d), however, we detect very similar offsets of B_0 for the first and second conductance plateaus. Therefore, we tentatively disregard the parity of the wave functions in the QPC to explain the observed offset in magnetic fields.

The experimentally determined values of b are depicted in Fig. 3(e). Surprisingly, they are 10 to 30 times larger than b_{Fermi} . Additionally, b does not significantly depend on E_{ph} , nor does it differ for the QPC tuned to the first or second conductance plateau. However, b increases with P_{laser} and thus with the density of the photogenerated electrons. In turn, electron-electron scattering most probably deflects the cyclotron traces of individual photogenerated electrons yielding an enlarged effective magnetic focusing radius, as discussed in the following.

IV. SIMULATION

Generally, the OBIC comprises electrons photogenerated at the source contact, which propagate across the QPC to the drain contact. We experimentally observe that the OBIC decays exponentially on a length scale l_{photo} , which is comparable to l_{mfp} .¹⁴ Therefore, the average transit time τ_{transit} of a resonantly excited electron from the laser spot to the QPC can be estimated to be $\tau_{\text{transit}} \approx \frac{l_{\text{photo}}}{v_{\text{Fermi}}} \approx \frac{l_{\text{mfp}}}{v_{\text{Fermi}}} = \frac{15.1 \mu\text{m}}{2.3 \times 10^5 \frac{\text{m}}{\text{s}}} \approx 66$ ps. At an excess energy ΔE of only a few meV above E_{Fermi} , the electron trajectories in 2DEGs are dominated by electron-electron scattering.^{16,17} The single particle electron-electron scattering time in 2DEGs is inversely proportional to $(\Delta E/E_F)^2 \ln(\Delta E/E_F)$, and for $\Delta E \sim$ meV, it is in the range of a few ps.²³ This relates to an unperturbed motion along only a few hundreds of nanometers, which is much shorter than l_{mfp} and r_{eff} presented here. Hence, photogenerated excess electrons can be assumed to scatter at a few electrons during τ_{transit} before they reach the QPC. We note that the energy distribution of photogenerated electrons approaching the QPC can be estimated to be a combination of a Gaussian and a Maxwell–Boltzmann distribution.^{24,25} Since we detect quantized photocurrent steps [Fig. 1(b)], an upper limit of the FWHM of this effective energy distribution can be assumed to be smaller than the 1D subband spacing of the QPC of

~ 4 meV¹⁴ for both quasi-resonant and nonresonant excitation. At $\Delta E = 49$ meV (nonresonant excitation), the photogenerated electrons strongly interact with longitudinal optical phonons. Due to both the phonon scattering and the enhanced electron-electron scattering for nonequilibrium charge carriers, the electrons effectively relax near the Fermi edge within a few picoseconds.²⁶ This substantially explains why there is no significant variation between the two photon energies.

Based upon these arguments, we perform Monte Carlo simulations to describe the enlarged magnetic focusing radii by the following simplified model. An electron resonantly created at the laser spot propagates at v_{Fermi} , and it obeys the Lorentz force. On top, the electron is scattered at other electrons with a rate τ_{ee}^{-1} on its way to the QPC. Each electron-electron scattering event deflects the k -vector of the electron at a certain small angle.^{27,28} In addition, the boundary of the 2DEG allows skipping orbits with a certain loss probability of p_{spec} . Figure 4(a) exemplifies two such trajectories which eventually reach the QPC. For each excitation position (x, y) , only a certain number of all possible trajectories reach the QPC, since the laser excitation creates electrons isotropically and the trajectories are exponentially weighted by the elastic mean free path in order to consider momentum scattering. This defines a hit rate $p_{\text{hit}} = p_{\text{hit}}(x, y, \mathbf{B})$, which is exemplarily plotted for certain simulation parameters in Fig. 4(b). Generally, we find that the simulations nicely reproduce the experimental data as in Fig. 2(a). In a next step, the simulated datasets are fitted with $h(x, y)$, and an effective magnetic focusing radius $r_{\text{eff}}^{\text{sim}}$ is extracted, analogous to the fitting procedure of the experimentally determined data. Again, we observe that

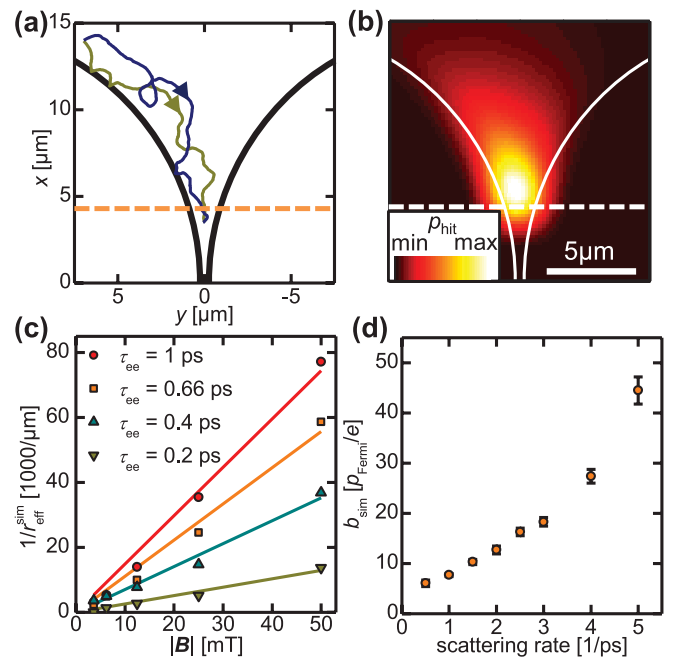


FIG. 4. (Color online) (a) Typical simulated trajectories with a common starting point. Black lines represent circuit boundaries. Dashed line indicates boundary of topgate. (b) Simulated spatial distribution of p_{hit} for $|\mathbf{B}| = 50$ mT and $\tau_{\text{ee}} = 0.66$ ps. (c) Extracted inverse of $r_{\text{eff}}^{\text{sim}}$ vs $|\mathbf{B}|$ for varying τ_{ee} . (d) Simulated inverse slopes b_{sim} vs scattering rate.

$r_{\text{eff}}^{\text{sim}}$ is inversely proportional to $|\mathbf{B}|$ [Fig. 4(c)]. The slopes in Fig. 4(c) depend on τ_{ee}^{-1} . In other words, $r_{\text{eff}}^{\text{sim}}$ reflects the number of electron-electron scattering events along the trajectories. A detailed evaluation of this dependence is shown in Fig. 4(d). Most importantly, the simulated values b_{sim} are up to 50 times larger than the anticipated b_{Fermi} . For a scattering rate in the range of $1 \frac{1}{\text{ps}} \leq \frac{1}{\tau_{\text{ee}}} \leq 3 \frac{1}{\text{ps}}$, b_{sim} agrees well with the experimentally determined values in Fig. 3(e), although the simulation does not contain any scaling parameter.

V. DISCUSSION

Strictly speaking, the assumed scattering mechanism is a generalized small-angle scattering including electron-electron scattering. However, we interpret the electron-electron scattering to dominate the rate τ_{ee}^{-1} by the following five arguments. First, the underlying scattering process relates to a length scale of typically ~ 100 nm, which is significantly shorter than l_{mfp} at low temperatures. Sample specific scattering potentials, which relate to l_{mfp} at low temperatures, are background dopants and remote (ionized or neutral) impurities.^{29–31} They are mainly screened at an increasing electron density. With increasing laser excitation intensity and a resulting higher overall electron density, these scatterers become more screened, and in turn, the corresponding scattering rate would be reduced. However, this is in contradiction to our findings for the laser power dependence, as presented in Fig. 3(e). Hereby, we can exclude sample-specific scattering processes to dominate the rate τ_{ee}^{-1} , although l_{mfp} is still a relevant parameter in our experiments. The latter can be seen by the decay of A_{OBIC} vs distance with a characteristic length $\delta_{\text{decay}} \sim l_{\text{mfp}}$.¹⁴ Second, there are two scenarios where electron-phonon interactions can influence the transport properties of 2DEGs: at elevated temperatures via phonon absorption and at a large enough excess energy of the electrons via phonon emission.^{32,33} The latter is also relevant at low temperatures. Optical phonons can be emitted at a rate in the order of ps^{-1} by electrons with an excess energy exceeding 36 meV at low temperatures.^{26,34,35} Such an excess energy, however, is clearly not achieved in our photocurrent measurements under quasi-resonant laser excitation at 8–10 K. In addition, we observe no significant difference between the quasi-resonant and nonresonant excitation. Therefore, optical phonons can be excluded to be of predominant influence to describe our results. In the case of acoustic phonons, the scattering rate is in the order of $(100 \text{ ps})^{-1}$ at low temperatures,³⁴ i.e. too low to explain our experiments as corroborated by the Monte Carlo simulations. Recent transport experiments in AlGaAs-based heterostructures confirmed such rather low rates for nonequilibrium electron beams.³⁶ Hereby, we can exclude both optical and acoustic phonons to be of predominant importance to describe our experiments on the nonequilibrium photogenerated electrons. Third, we calculate the energy difference between the first and second subband due to the z quantization to be $E_{2\text{ndSUB}} - E_{1\text{stSUB}} = 21 \text{ meV}$.¹⁴ For quasi-resonant (nonresonant) excitation, we use a photon energy of $E_{\text{ph}} = 1.546 \text{ eV}$ (1.598 eV) with an FWHM of both lasers of 8 meV. Thus, at least for quasi-resonant excitation, no electrons are generated in the second subband. The second subband should only come into play at very high excitation powers. However, even then we do not detect

any indication for such dynamics. As we do not see a qualitative difference between quasi-resonant and nonresonant excitation for the magnetic focusing experiments, we exclude intersubband scattering as a predominant effect to describe our results.³⁷ Fourth, the large value of r_{eff} could also point towards spin-orbit coupling³⁸ or collective phenomena such as plasmons or charge density waves.^{39,40} Both can influence the screening of the lattice, affecting m^* , and the screening of scatterers, as has been reported for low-temperature-grown GaAs.^{39,41} Collective phenomena, however, cannot account for an increase of 30 times. Furthermore, to launch plasmons via the laser excitation, one would need a certain k -vector component in the in-plane direction which we do not have. We calculate the threshold excess energy for plasmon emission to be 20 meV above E_{F} .¹⁷ Again, since quasi-resonant and nonresonant excitation yield qualitatively equivalent results, we can exclude plasmons to have a dominant influence on the presented experiment. Finally, we can also exclude streaming motion to be the underlying reason for our experimental findings⁴² because it occurs only in crossed electric and magnetic fields, which can be assumed not to be the case at the positions of the laser excitation [Figs. 1(c)–1(f)]. Furthermore, assuming a macroscopic (diffusive) Hall circuit with crossed electric and magnetic fields, the classical Hall angle reads $\theta_{\text{Hall}} = \arctan(\mu|\mathbf{B}|)$. For the given μ and a magnetic field of $|\mathbf{B}| = 10 \text{ mT}$, θ_{Hall} would already be 60° . Generally, in a notional diffusive regime, the charge carriers are deflected with a direction given by θ_{Hall} , which we do not detect in our OBIC maps [Figs. 1(e) and 1(f)].

Based upon these arguments, we interpret the electron-electron scattering to explain our findings. The extracted range $1 \frac{1}{\text{ps}} \leq \frac{1}{\tau_{\text{ee}}} \leq 3 \frac{1}{\text{ps}}$ is at most one order of magnitude larger than findings reported by Schäpers *et al.* on nonequilibrium electron transport without laser excitation at slightly lower temperatures.²⁵ However, in contrast to both the experiments by Schäpers *et al.* and previous magnetic focusing experiments,^{5–7} our measurements exclusively concentrate on the propagation paths of additional photogenerated, nonequilibrium excess electrons. They have a softened energy distribution compared to the one of the thermalized, nonexcited electrons and thus an enlarged phase space for electron-electron scattering compared to a completely degenerate electron ensemble.²⁴ This is a significant difference such that photogenerated electrons experience an increased electron-electron scattering compared to thermalized nonexcited electrons. Hereby, in combination with the relatively high temperature in our photoinduced nonequilibrium experiments and an excess energy of up to $\Delta E = 8 \text{ meV}$ even for quasi-resonant excitation (because of the FWHM of the laser), we explain the slightly increased scattering rate compared to Ref. 25. We would like to stress that, in principle, any scattering process via an energy quantum larger than $\sim 4 \text{ meV}$ may contribute to the scattering of the photogenerated electrons satisfying the simulated high rates above 1 ps^{-1} (with the energy of $\sim 4 \text{ meV}$ the 1D subband spacing of the QPC as the detector). Following the arguments mentioned above, however, we tentatively attribute the electron-electron scattering to largely explain our results.

We note that such a conclusion is consistent with recent findings by Molenkamp *et al.* on nonequilibrium electron ensembles.⁴³ They could experimentally verify a dominating

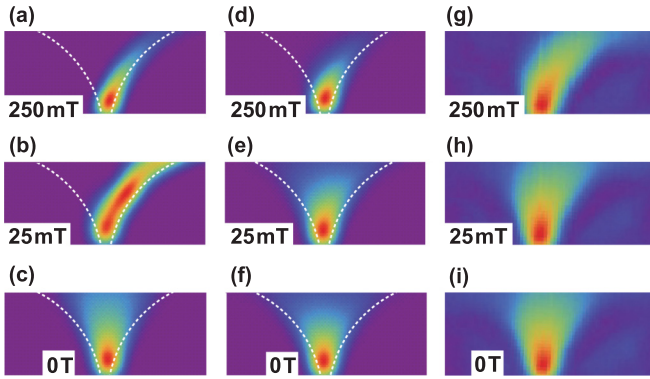


FIG. 5. (Color online) Measurements and simulations for magnetic fields of 250 mT, 25 mT, and 0 T. (a)–(c) Simulations without small angle scattering, but boundary reflection. (d)–(f) Simulations with both small angle scattering and boundary scattering for a scattering time of 0.4 ps. (g)–(i) Measured OBIC maps ($E_{\text{ph}} = 1.598$ eV, $V_G = 280$ mV, $V_{\text{SD}} = -2.5$ mV, $P_{\text{laser}} = 1.0$ μ W).

electron-electron scattering mechanism to describe the heating mechanism of a nonequilibrium electron ensemble by current and hot electron injection compared to a phonon-induced crystal lattice heating. Along this line, we show simulations without small angle scattering within the electronic system in Figs. 5(a)–5(c). Here, the electrons move in skipping orbits along the boundary already for $|\mathbf{B}| \geq 25$ mT. In turn, the photocurrent flow patterns are located very close to the edges of the 2DEG [Figs. 5(a) and 5(b)]. Only via the introduction of small angle scattering into the simulations [Figs. 5(d), 5(e), and 5(f)], the measured OBIC maps can be reproduced [Figs. 5(g), 5(h), and 5(i)]. We point out that momentum conservation of the whole photogenerated electron ensemble is not necessarily fulfilled in the experiment, since not all electrons initially created by the laser position are detected at the QPC. For the sake of computation time, only the trajectories of individual photogenerated electrons within the electron bath are calculated, without considering the momentum conservation of the whole photogenerated electron ensemble.

We finally note that the data in Fig. 3(e) suggest an enlarged r_{eff} even at $P_{\text{laser}} = 0$. This is consistent with the fact that small angle scattering, including electron-electron scattering, is present in the 2DEG also without laser excitation.^{22,25}

VI. CONCLUSIONS

In summary, we analyze the magnetic focusing of photogenerated excess charge carriers in a GaAs 2DEG. By applying a photocurrent mapping technique to mesoscopic circuits with a quantum point contact as a local photocurrent detector, we spatially resolve the photocurrent flow patterns in a 2DEG at a perpendicular magnetic field. Initially assuming that the electronic motion can be classically described with cyclotron orbits, we model the data with a two-dimensional fitting function that enables us to extract an effective radius as a fitting parameter. Surprisingly, we find that the measured values lie significantly above the expected values. By analyzing the laser power dependence of our signal and performing Monte Carlo simulations, we attribute the enlarged magnetic focusing radius

to an enhanced scattering of the photogenerated electrons, in particular electron-electron scattering, which is a unique fingerprint of optoelectronic experiments.

ACKNOWLEDGMENTS

We thank A. Högele for technical support and G. J. Schinner, A. Govorov, and L. Prechtel for fruitful discussions. Financial support from the German Science Foundation DFG (Ho 3324/4), the Center for NanoScience (CeNS), and the German excellence initiative via the “Nanosystems Initiative Munich (NIM)” is gratefully acknowledged. M. Stallhofer gratefully acknowledges the support of the TUM Graduate School’s Faculty Graduate Center of Physics at the Technische Universität München.

APPENDIX: SIMULATION DETAILS

The Monte Carlo simulations are performed as discussed in the following. Firstly, the source contact is represented as a rectangular grid. The size of this grid is 20 μm in y direction ($-10; 10$) and 10 μm in x direction ($0; 10$) with a grid step size of 0.25 μm . Each grid point denotes a position vector $\vec{r} = \begin{pmatrix} x \\ y \end{pmatrix}$. The sample design is introduced by implementing circuit boundaries with a certain reflectivity (specularity) $0 \leq p_{\text{spec}} \leq 1$ with typical values around $p_{\text{spec}} = 0.8$, as recently discussed in Ref. 44. The detector QPC is defined as the funnel-shaped end region of the circumference of the grid. If a particle reaches an x value smaller than 4 μm , it is assumed to be collected by the QPC.

From each grid point, electrons initially start with a randomly directed velocity vector $|\vec{v}| = 0.2 \frac{\mu\text{m}}{\text{ps}}$ (Fermi velocity). After each time period $\Delta t = 0.2$ ps, electrons will encounter another electron, and they will be scattered by a randomly chosen angle α uniformly distributed within the interval $10^\circ \leq |\alpha| \leq 30^\circ$ with a probability p . The value for the angle distribution is estimated from Fig. 4(a) in Ref. 27. This simple model assumes that an electron has a spatial extension of its de Broglie wavelength in average. For an electron density of $n = 2.75 \times 10^{11}$ cm^{-2} , the de Broglie wavelength is 48 nm. Between two electron scattering processes, the trajectory is influenced by the magnetic field, and thus, the path will always be deflected by an angle $\alpha_{\text{mag}} = \frac{|\vec{v}| \Delta t}{r_{\text{cyclo}}} \frac{360^\circ}{2\pi}$. In the presented simulation, fields up to ± 50 mT are assumed, corresponding to a minimum classical cyclotron orbit of $r_{\text{cyclo}} = 1.74$ μm . The influence of the magnetic field is implemented by rotating the velocity vector after each time interval Δt by α_{mag} , additionally to the random rotation due to scattering. If a trajectory reaches the detector within a certain maximum number of time intervals $N \leq 2000$ (equivalent to a maximum total distance of $s_{\text{max}} = |\vec{v}| \Delta t N_{\text{max}} = 80$ μm), it is registered as a hit. The contribution of each individual trace that reaches the detector to the accumulated count for its starting point is exponentially weighted with the elastic mean free path to take momentum scattering into account. To account for nonperfectly reflecting (absorbing) boundaries of the circuit, we additionally multiply the final value for each trajectory with a number $(p_{\text{spec}})^{N_{\text{boundary}}}$ (N_{boundary} : number of boundary hits). In the simulation, 100 traces are started from each

point of the grid. The simulated raw data are convoluted with a Gaussian kernel with $\sigma = 1 \mu\text{m}$ to account for the laser broadening in the experiment. Plotting the number of hits for each point as a two-dimensional contour plot, one acquires a simulated distribution as shown in Fig. 4(b), very similar to the experimental data. To extract spatial information

about the simulated distribution, we use the same fitting algorithm to extract the effective radius $r_{\text{eff}}^{\text{sim}}$ that we compare with the experimentally determined effective radius r_{eff} of the photocurrent flow patterns. Finally, we point out that the qualitative outcome of the simulations does not depend on the exact range of α , as long as a small angle scattering is assumed.

- ¹See e.g., P. Stallhofer, J. P. Kotthaus, and G. Abstreiter, *Solid State Commun.* **32**, 655 (1979) and references therein.
- ²W. Kohn, *Phys. Rev.* **123**, 1242 (1961).
- ³B. J. van Wees, H. van Houten, C. W. J. Beenakker, J. G. Williamson, L. P. Kouwenhoven, D. van der Marel, and C. T. Foxon, *Phys. Rev. Lett.* **60**, 848 (1988).
- ⁴D. A. Wharam, T. J. Thornton, R. Newbury, M. Pepper, H. Ahmed, J. E. F. Frost, D. Hasko, D. C. Peacock, D. A. Ritchie, and G. A. C. Jones, *J. Phys. C* **21**, L209 (1988).
- ⁵H. van Houten, C. W. J. Beenakker, J. G. Williamson, M. E. I. Broekaart, P. H. M. van Loosdrecht, B. J. van Wees, J. E. Mooij, C. T. Foxon, and J. J. Harris, *Phys. Rev. B* **39**, 8556 (1989).
- ⁶J. Spector, J. S. Weiner, H. L. Stormer, K. W. Baldwin, L. N. Pfeiffer, and K. W. West, *Surf. Sci.* **263**, 240 (1992).
- ⁷R. Crook, C. G. Smith, M. Y. Simmons, and D. A. Ritchie, *Phys. Rev. B* **62**, 5174 (2000).
- ⁸K. E. Aidala, R. E. Parrot, T. Kramer, E. J. Heller, R. M. Westervelt, M. P. Hanson, and A. C. Gossard, *Nature Phys.* **3**, 464 (2007).
- ⁹M. A. Topinka, B. J. LeRoy, S. E. J. Shaw, E. J. Heller, R. M. Westervelt, K. D. Maranowski, and A. C. Gossard, *Science* **289**, 2323 (2000).
- ¹⁰M. A. Topinka, B. J. LeRoy, R. M. Westervelt, S. E. J. Shaw, R. Fleischmann, E. J. Heller, K. D. Maranowski, and A. C. Gossard, *Nature* **410**, 183 (2001).
- ¹¹B. J. LeRoy, A. C. Bleszynski, K. E. Aidala, R. M. Westervelt, A. Kalben, E. J. Heller, S. E. J. Shaw, K. D. Maranowski, and A. C. Gossard, *Phys. Rev. Lett.* **94**, 126801 (2005).
- ¹²M. P. Jura, M. A. Topinka, M. Grobis, L. N. Pfeiffer, K. W. West, and D. Goldhaber-Gordon, *Phys. Rev. B* **80**, 041303(R) (2009).
- ¹³I. Neder, N. Ofek, Y. Chung, M. Heiblum, D. Mahalu, and V. Umansky, *Nature* **448**, 333 (2007).
- ¹⁴K. D. Hof, F. J. Kaiser, M. Stallhofer, D. Schuh, W. Wegscheider, P. Hänggi, S. Kohler, J. P. Kotthaus, and A. W. Holleitner, *Nano Lett.* **10**, 3836 (2010).
- ¹⁵K. D. Hof, C. Rossler, S. Manus, J. P. Kotthaus, A. W. Holleitner, D. Schuh, and W. Wegscheider, *Phys. Rev. B* **78**, 115325 (2008).
- ¹⁶A. V. Chaplik, *Zh. Eksp. Teor. Fiz.* **60**, 1845 (1971) [*Sov. Phys.* **33**, 997 (1971)].
- ¹⁷G. F. Giuliani and J. J. Quinn, *Phys. Rev. B* **26**, 4421 (1982).
- ¹⁸M. P. Jura, M. Grobis, M. A. Topinka, L. N. Pfeiffer, K. W. West, and D. Goldhaber-Gordon, *Phys. Rev. B* **82**, 155328 (2010).
- ¹⁹A. Szafer and A. D. Stone, *Phys. Rev. Lett.* **62**, 300 (1989).
- ²⁰M. P. Jura, M. A. Topinka, L. Urban, A. Yazdani, H. Shtrikman, L. N. Pfeiffer, K. W. West, and D. Goldhaber-Gordon, *Nature Phys.* **3**, 841 (2007).
- ²¹D. Többen, D. A. Wharam, G. Abstreiter, J. P. Kotthaus, and F. Schäffler, *Phys. Rev. B* **52**, 4704 (1995).
- ²²K. E. Aidala, R. E. Parrot, E. J. Heller, and R. M. Westervelt, *Physica E* **34**, 409 (2006).
- ²³A. Yacoby, U. Sivan, C. P. Umbach, and J. M. Hong, *Phys. Rev. Lett.* **66**, 1938 (1991).
- ²⁴D. W. Snoke, W. W. Rühle, Y. C. Lu, and E. Bauser, *Phys. Rev. Lett.* **68**, 990 (1992).
- ²⁵T. Schäpers, M. Krüger, J. Appenzeller, A. Förster, B. Lengeler, and H. Lüth, *Appl. Phys. Lett.* **66**, 3603 (1995).
- ²⁶J. Shah, *Ultrafast Spectroscopy of Semiconductors and Semiconductor Nanostructures*, 2nd ed. (Springer, Berlin Heidelberg, 1999).
- ²⁷A. V. Yanovsky, H. Predel, H. Buhmann, R. N. Gurzhi, A. N. Kalinenko, A. I. Kopeliovich, and L. W. Molenkamp, *Europhys. Lett.* **56**, 709 (2001).
- ²⁸D. R. S. Cumming and J. H. Davies, *Appl. Phys. Lett.* **69**, 3363 (1996).
- ²⁹R. Dingle, H. L. Störmer, A. C. Gossard, and W. Wiegmann, *Appl. Phys. Lett.* **33**, 665 (1978).
- ³⁰W. Walukiewicz, H. E. Ruda, J. Lagowski, and H. C. Gatos, *Phys. Rev. B* **30**, 4571 (1984).
- ³¹H. L. Störmer, *Surf. Sci.* **132**, 519 (1983).
- ³²B. Vinter, *Appl. Phys. Lett.* **45**, 581 (1984).
- ³³U. Sivan, M. Heiblum, and C. P. Umbach, *Phys. Rev. Lett.* **63**, 992 (1989).
- ³⁴U. Bockelmann and G. Bastard, *Phys. Rev. B* **42**, 8947 (1990).
- ³⁵D. Taubert, C. Tomaras, G. J. Schinner, H. P. Tranitz, W. Wegscheider, S. Kehrein, and S. Ludwig, *Phys. Rev. B* **83**, 235404 (2011).
- ³⁶G. J. Schinner, H. P. Tranitz, W. Wegscheider, J. P. Kotthaus, and S. Ludwig, *Phys. Rev. Lett.* **102**, 186801 (2009).
- ³⁷H. L. Störmer, A. C. Gossard, and W. Wiegmann, *Surf. Sci.* **41**, 707 (1982).
- ³⁸J. Schliemann, *Phys. Rev. B* **77**, 125303 (2008).
- ³⁹I. Baskin, B. M. Ashkinadze, E. Cohen, and L. N. Pfeiffer, *Phys. Rev. B* **84**, 041305 (2011).
- ⁴⁰G. Grüner, *Rev. Mod. Phys.* **60**, 1129 (1988).
- ⁴¹G. A. Khodaparast, D. C. Larrabee, J. Kono, D. S. King, S. J. Chung, and M. B. Santos, *Phys. Rev. B* **67**, 035307 (2003).
- ⁴²S. Komiyama, *Adv. Phys.* **31**, 255 (1982).
- ⁴³L. W. Molenkamp, M. J. P. Brugmans, H. van Houten, and C. T. Foxon, *Semicond. Sci. Technol.* **7**, B228 (1992).
- ⁴⁴M. J. M. de Jong and L. W. Molenkamp, *Phys. Rev. B* **51**, 13389 (1995).